iScience

CellPress
OPEN ACCESS

Article

Zr modulated N doping composites for CO_2 conversion into carbonates

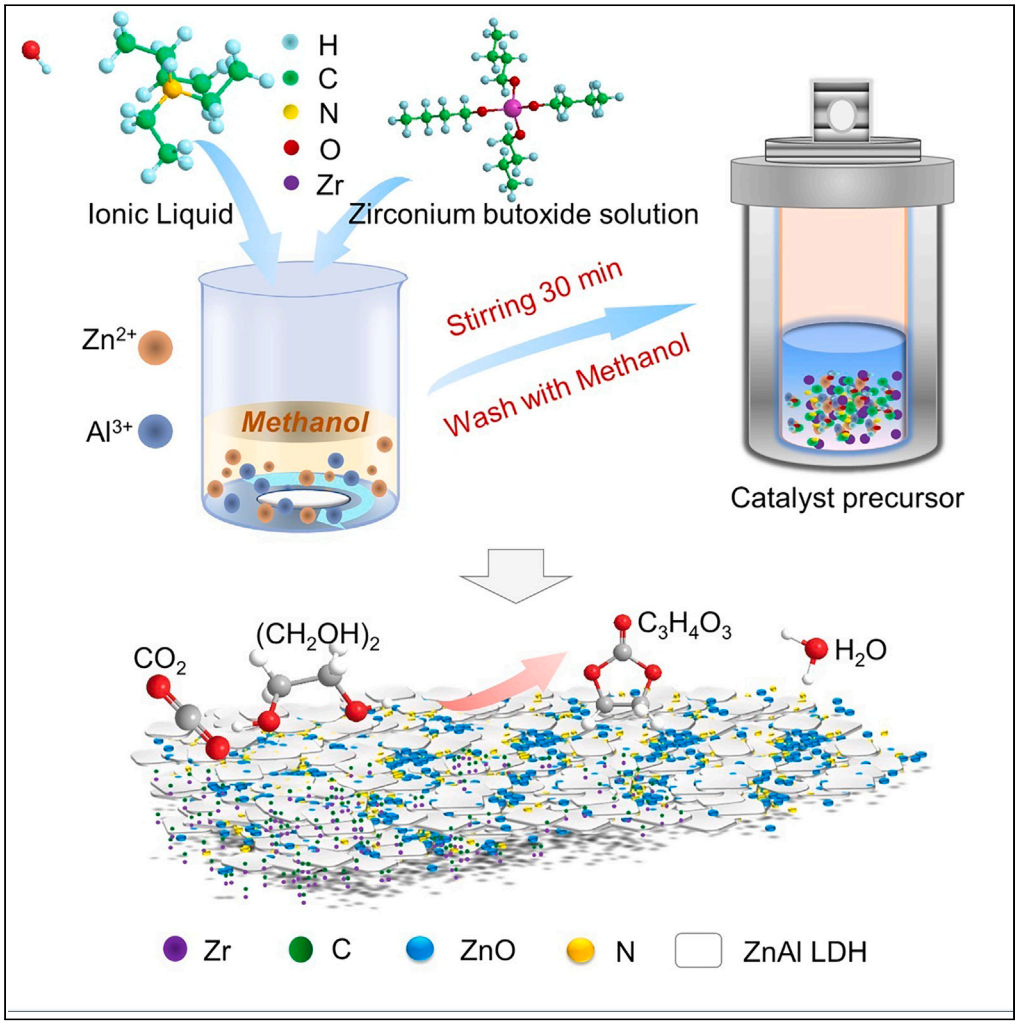

Jielin Huang, Jie Wang, Haonan Duan, Li Dong, Songsong Chen, Junping Zhang, Xiangping Zhang

ldong@ipe.ac.cn (L.D.)
zhangjp@ipe.ac.cn (J.Z.)
xpzhang@ipe.ac.cn (X.Z.)

Highlights

The LDHs were prepared directly in ionic liquid and methanol systems

N, C, and ZnO doping was achieved during the preparation process

Higher pyridinic-N content increased the strong basic sites of the material

The catalytic performance of the samples is up to 4.76 $mmol_{EC}\ g_{Cat.}^{-1}\ h^{-1}$

Huang et al., iScience 27, 109714
May 17, 2024
https://doi.org/10.1016/j.isci.2024.109714

iScience

CellPress
OPEN ACCESS

Article

Zr modulated N doping composites for CO_2 conversion into carbonates

Jielin Huang,[1,2] Jie Wang,[1,2] Haonan Duan,[2] Li Dong,[1,2,3,4,*] Songsong Chen,[2] Junping Zhang,[2,3,*] and Xiangping Zhang[2,3,*]

SUMMARY

Acidic and basic sites of catalysts are essential for CO_2 capture and activation. In this work, Zr, N-ZnO/ZnAl-LDH-IL composites in ionic liquid and methanol systems were fabricated, and applied to catalyze the synthesis of ethylene carbonate (EC) from ethylene glycol (EG) and CO_2 with about 4.76 $mmol_{EC}$ $g_{Cat.}^{-1}$ h^{-1}. The composites showed more strong basic sites due to the effective induction of reactive groups on the catalyst surface by Zr doping, resulting in an increase of pyridinic-N groups from 5.48% to 22.25%. More C atoms adjacent to pyridinic-N as strong basic sites was conducive to the activation of CO_2 and EG. In addition, the possible catalytic pathway and mechanism of the composites for synthesizing EC as well as the doping of La, Fe, Ce, and Cu were also investigated, which provides an effective strategy for regulating the acid-base centers on the catalyst surface through ionic liquids and methanol solvents.

INTRODUCTION

Carbon dioxide (CO_2) produced in daily human life and industrial production has become an increasingly serious global issue in recent years and gradually threatens the survival environment of human.[1–3] As a safe and abundant C1 resource, CO_2 is an essential raw material for synthesizing significant chemicals such as formic acid, methanol, carbonates, carbamates, and carboxylic acids.[4–7] Therefore, the effective conversion of CO_2 into carbonates is a highly valuable area of research.

Ethylene carbonate (EC) is an essential electrolyte for lithium-ion batteries, and widely employed in textiles, printing and dyeing, polymer synthesis, and other applications.[6–8] The phosgene process is the traditional method for producing EC, which has become obsolete due to the disadvantages of low yield, long cycle time, high costs, and heavy pollution.[9] The preparation of EC from CO_2 and ethylene oxide is the current industrial production method, but the safety problem exists with this reaction. Besides, with the surplus of coal-based ethylene glycol (EG), there is an increasing need for a new technology to convert EG into higher value chemicals. Thereby, the direct synthesis of carbonates from alcohols and CO_2, such as the preparation of EC using CO_2 and EG, shows excellent advantages in industrial production including fewer production costs and more straightforward production routes. Nevertheless, the research on the direct preparation of EC from CO_2 and EG without the addition of solvents remains challenging. According to literature reports, the types of catalysts reported for converting CO_2 and EG to EC are few, and limited to CeO_2, ZrO_2, and several organocatalysts, which catalyze the reaction process in a solvent.[10–14] In conclusion, the design and preparation of catalysts with excellent catalytic activity is currently a major research hotspot.

Zinc-aluminum layered double hydroxide (ZnAl-LDH) has recently become a hot material owing to the features of good dispersibility, multifunctionality, high plasticity, and low cost.[15] The synthesis process of materials was carried out in methanol, 2-methylimidazole and ethanol, and the change in the formation environment of materials leads to the synthesis of materials with different physical and chemical properties, thereby improving the catalytic performance of ZnAl-LDH materials.[16–18] The unique properties of ionic liquids (ILs) including low interfacial tension, high viscosity, and high electrical conductivity, can all influence the preparation of catalytic materials, which offers a variety of possibilities for the acquisition of advanced catalytic materials.[19] For synthesizing EC from EG and CO_2, the deprotonation of alcohol hydroxyl group is the key step, and the ability of the catalyst to catalyze the deprotonation of alcohols is enhanced by non-metals doping, the direct interaction of metal oxides with homogeneous components, the modification of solvents, and the introduction of functional groups.[15] Moreover, the Lewis basic sites are meaningful for hydrogen extraction and proton release.[20] N-doping of carbon-containing materials enables different types of N-containing functional groups in the material, promoting the formation of Lewis basic sites.[21] The catalytic efficiency of catalysts by varying the ratio of pyridinic-N to pyrrolic-N in the material was investigated, and pyridinic-N played a more critical role in forming

[1]School of Chemical Engineering, University of Chinese Academy of Sciences, Beijing 100049, China
[2]Beijing Key Laboratory of Ionic Liquids Clean Process, CAS Key Laboratory of Green Process and Engineering, State Key Laboratory of Mesoscience and Engineering, Institute of Process Engineering, Chinese Academy of Sciences, Beijing 100190, China
[3]Advanced Energy Science and Technology Guangdong Laboratory, Huizhou, Guangdong 516003, China
[4]Lead contact
*Correspondence: ldong@ipe.ac.cn (L.D.), zhangjp@ipe.ac.cn (J.Z.), xpzhang@ipe.ac.cn (X.Z.)
https://doi.org/10.1016/j.isci.2024.109714

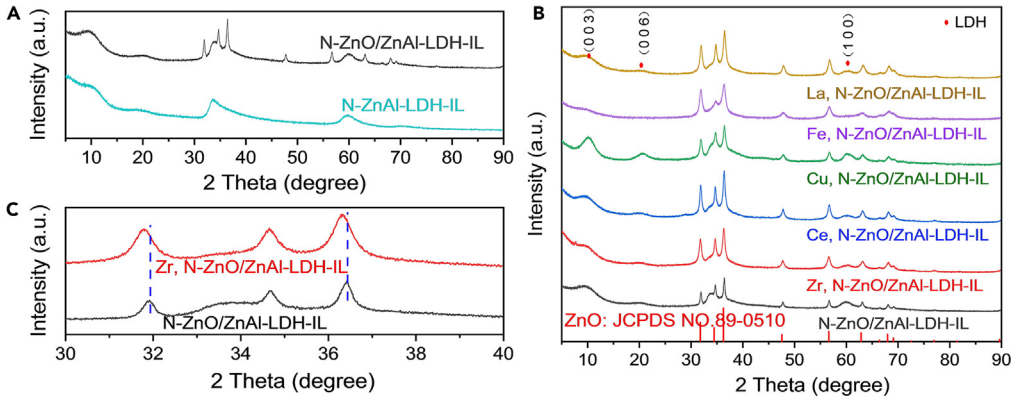

Figure 1. XRD patterns of all samples

(A) XRD patterns of the N-ZnAl-LDH-IL and N-ZnO/ZnAl-LDH-IL samples.

(B) XRD patterns of N-ZnO/ZnAl-LDH-IL and different metal-doped N-ZnO/ZnAl-LDH-IL composites.

(C) XRD patterns of partially enlarged profiles of 30–40° in (B).

Lewis basic sites than pyrrolic-N.[21–23] However, there are no reports on the formation of direct synthesis of LDH in IL/methanol system, such as the preparation of ZnAl-LDH with high specific surface area and *in situ* formation of ZnO with N doping.

A new and improved synthesis method by the introduction of ILs into methanol solution was developed, which contained Zn^{2+} and Al^{3+} to fabricate N and ZnO doped ZnAl-LDH composites for enhancing Lewis basic sites of materials and the preparation of EC from CO_2 and EG. The microenvironment of N-doped catalysts was influenced by Zr, Cu, Fe, La, or Ce doped, and the catalytic properties of the composites were also altered. Besides, Zr and doped N-ZnO/ZnAl-LDH-IL composites maintained the high specific surface area, which induced the variation in the N-group and the formation of Lewis basic sites compared with pristine ZnAl-LDH-IL and N-ZnO/ZnAl-LDH-IL catalysts, which enhanced the catalytic performance. The reaction pathway for preparing EC from CO_2 and EG under solvent-free conditions, as well as the synergistic catalysis mechanism of Lewis acid-base sites of the prepared Zr, N-ZnO/ZnAl-LDH-IL composites were proposed in detail, which also indicated that the synthesis of other N-doped layered porous materials for CO_2 conversion and utilization may be an effective strategy.

RESULTS AND DISCUSSION

Structural and morphology analysis

The formation and crystallized properties of N-ZnO/ZnAl-LDH-IL and metal-doped N-ZnO/ZnAl-LDH-IL composites were determined by powder X-ray diffraction. As displayed in Figure 1A, the prepared N-ZnAl-LDH-IL and N-ZnO/ZnAl-LDH-IL composites exhibited relatively weak diffraction peaks at 2θ = 9.1°, 18.9°, and 59.6°, which corresponded to (0 0 3), (0 0 6), and (1 0 0) planes of typical LDH phase, respectively. Besides, the samples showed weak signal peaks, mainly attributed to the synthesis process carried out in organic solvents.[16,24,25] From Figure 1B, relatively strong diffraction peaks located at approximately 31.88°, 34.67°, 36.31°, 47.75°, 56.70°, 63.11°, 68.10°, and 69.17° were observed in the N-ZnO/ZnAl-LDH-IL and Zr, N-ZnO/ZnAl-LDH-IL composites, which agreed well with the standard joint committee on powder diffraction standards (JCPDS) card of ZnO (JCPDS No. 89–0510) and represented the (1 0 0), (0 0 2), (1 0 1), (1 0 2), (1 1 0), (1 0 3), (0 0 2), (1 1 2) and (2 0 1) planes of ZnO, further demonstrating the successful fabrication of the N-ZnAl-LDH-IL composites with *in situ* generation of ZnO.[16] Furthermore, the N-ZnO/ZnAl LDH IL composites material doped with Ce, Cu, Fe, and La exhibited typical diffraction peaks of LDH phases (0 0 3), (0 0 6), and (1 1 0), and metal doping had no effect on the *in-situ* formation of ZnO from N-ZnAl LDH IL material. Moreover, the diffraction peak characteristics of N-ZnO/ZnAl-LDH-IL and Zr, N-ZnO/ZnAl-LDH-IL samples in the 2θ range of 30–40° were presented in Figure 1C, and the diffraction peaks of the Zr, N-ZnO/ZnAl-LDH-IL materials corresponding to the 2θ = 31.88° and 36.31° positions shifted toward a smaller angle due to the successful doping of Zr, which resulted in a change in the exposed surface of ZnO at (1 0 0) and (1 0 1) planes.[26,27]

The functional groups of the prepared N-ZnAl-LDH-IL, N-ZnO/ZnAl-LDH-IL, and Zr, N-ZnO/ZnAl-LDH-IL composites were determined by fourier transform infrared spectroscopy (FT-IR) test. As shown in Figure 2, strong absorption bands belonging to $V_{N\text{-}H}$ at 3500 cm^{-1} of all N-doped composites were observed, and the absorption peak of Zr, N-ZnO/ZnAl-LDH-IL sample was sharper at 3500 cm^{-1} compared to N-ZnAl-LDH-IL and N-ZnO/ZnAl-LDH-IL composites, which suggested that Zr doping led to the formation of free $V_{N\text{-}H}$ groups. The characterized peaks at 3430 cm^{-1} and 1620 cm^{-1} originated from the stretching vibrations of -OH groups and water molecules between the ZnAl-LDH layers, and a strong peak at 1389 cm^{-1} was detected, which depicted the vibration of the Zn-N bond, confirming the incorporation of N into the ZnO.[22,28,29] Compared to the N-ZnAl-LDH-IL and N-ZnO/ZnAl-LDH-IL samples, a narrower absorption peak of the Zr, N-ZnO/ZnAl-LDH-IL composites appeared at 1390 cm^{-1}, probably because of the dissociation of multiple Zn-N bonds to form a Lewis basic N^- site.[22] The intense band at 1347 cm^{-1} was associated with the ν_3 stretching mode of NO_3^-, and the absorption band at 1176 cm^{-1} belonged to the vibrational peak of the C-*O*-C bond. In addition, the peak at 1041 cm^{-1} mainly resulted from the nitrate or hyponitrite group, and absorption bands around 450 cm^{-1} to 800 cm^{-1} were attributed to the vibrations of the M-O, M-*O*-M and O-*M*-O bonds.[30] Hence, Zr doping on N-ZnO/ZnAl-LDH-IL

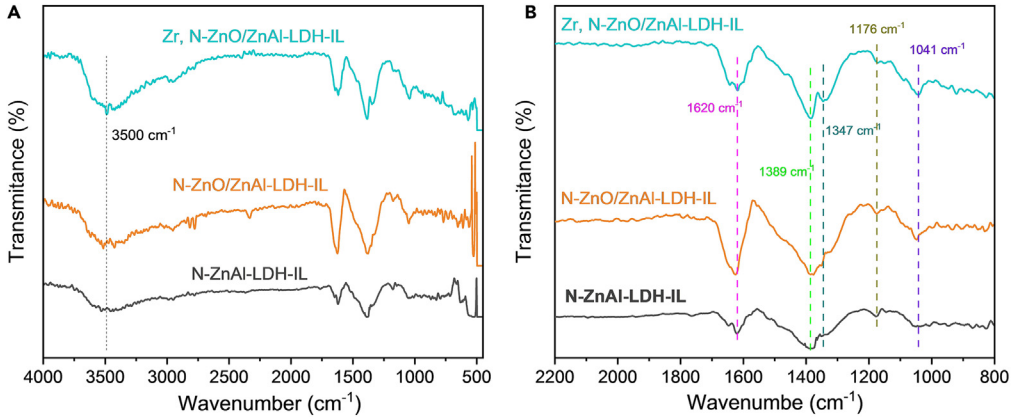

Figure 2. FT-IR spectra of the samples

(A) FT-IR spectra of N-ZnAl-LDH-IL, N-ZnO/ZnAl-LDH-IL, and Zr, N-ZnO/ZnAl-LDH-IL samples.

(B) FT-IR spectra of partially enlarged profiles of 2200-800 cm^{-1} in (A).

composites was achieved with an IL-assisted synthesis strategy in methanol. Besides, thermal gravimetric analyzer (TGA) and differential thermogravimetric analyses (DTG) analysis are also conducted to investigate the thermal stability and the content of carbon in the prepared sample, as shown in Figure S1. The evaporation of weakly adsorbed water molecules on the microcrystalline surface occurs mainly between 0°C and 150°C, the evaporation of interlayer embedded water between 150°C and 250°C, and the dehydroxylation and transition metal oxide crystallization and anionic substance decomposition occurs mainly between 250°C and 310°C.[9,16,17,30] As we know, the boiling point of tetraethylammonium hydroxide is at 110°C, and it can be seen in the figure that the rate of weight loss of the catalyst does not accelerate around 110°C, which indicates that there is almost no residual tetraethylammonium hydroxide on the catalyst surface. This suggests that the doping of the catalyst surface with non-metallic elements comes mainly from small molecular alcohols and the decomposition of ILs.

The morphology and nanostructures of the prepared Zr, N-ZnO/ZnAl-LDH-IL composites were recorded by transmission electron microscope (TEM), and the detailed TEM images of the prepared Zr, N-ZnO/ZnAl-LDH-IL composites with different magnifications were drawn in Figures 3A–3C. Similarly, prominent laminar features of Zr, N-ZnO/ZnAl-LDH-IL and uniform distribution of ZnO in the sample were found (see Figure 3A).[31,32] The composites showed a stacked porous lamellar character rather than a regular nanosheet structure like other ZnAl-LDHs, probably because of the synthesis environment of the N-ZnO/ZnAl-LDH-IL composites (methanol and tetraethyl ammonium hydroxide), as well as the fact that materials with this lamellar porous structure often possessed a large specific surface area.[15,16,33,34] Additionally, an image of the material at the 10 nm scale was also shown in Figure 3D, which indicated that the N-ZnO/ZnAl-LDH-IL composites were prepared by stacking of nanosheets and exhibited two types of lattice stripes of approximately 0.2533 and 0.2838 nm involved the 101 and 100 facets of ZnO, respectively, reflecting the *in situ* doping and homogeneous distribution.[35] Besides, the elemental mappings of the prepared Zr, N-ZnO/ZnAl-LDH-IL composites were investigated, and the prepared Zr, N-ZnO/ZnAl-LDH-IL composites catalysts were mainly composed of Zn, Al, O, N, C, and Zr elements, which could be seen from the elemental distribution overlay (Figure 3F). Figures 3G–3K showed the Al, O, Zn, N, and C distribution on the Zr, N-ZnO/ZnAl-LDH-IL samples in that order, and the enrichment of the elements on the samples suggested that the catalyst was mainly composed of Zn, Al, and O with N and C uniformly doped on the catalyst, where N and C exhibited similar distributions on the samples. In Figure 3L, the uniform distribution of element Zr over the catalyst suggested the uniform doping of Zr on N-ZnO/ZnAl-LDH-IL sample.[27,34] In conclusion, ILs and methanol were responsible for inducing the formation of ZnO/ZnAl-LDH-IL composites and promoting the uniform doping of N, C, and Zr.

Besides, the physical properties of Zr, N-ZnO/ZnAl-LDH-IL composites, such as the surface area and pore size distribution, were also determined by N_2 adsorption-desorption measurements in this work. As seen in Figure 4A, the type IV isotherms with H2 hysteresis loops were found for the prepared N-ZnAl-LDH-IL, N-ZnO/ZnAl-LDH-IL, and Zr, N-ZnO/ZnAl-LDH-IL composites, and the pore sizes of that were in the range of 3–6.7 nm (Figure 4B), which indicated the formation of mesopores in the composites.[36–38] Furthermore, the average pore size of the three samples was approximately 3.8 nm, and the N-ZnO/ZnAl-LDH-IL and Zr, N-ZnO/ZnAl-LDH-IL composites had a larger pore volume of roughly 0.17 $cm^3\ g^{-1}$ compared to the N-ZnAl-LDH-IL sample. As presented in Table 1, the surface areas of N-ZnAl-LDH-IL, N-ZnO/ZnAl-LDH-IL, and Zr, N-ZnO/ZnAl-LDH-IL composites were approximately 192.049, 183.087, and 205.542 $m^2\ g^{-1}$. Notably, the Zr doping did not result in a decrease in the specific surface area of N-ZnO/ZnAl-LDH-IL, but rather slightly increased by about 22.3 $m^2\ g^{-1}$. Accordingly, the preparation of N-ZnAl-LDH-IL composites in ILs and methanol while doping with ZnO and Zr maintained the microscopic LDH material structure.

Optical properties and surface composition

The optical properties of the catalysts were reported in Figure 5. In detail, Figure 5A showed the UV-Vis diffuse reflectance spectra (UV-vis DRs) of N-ZnAl-LDH-IL, N-ZnO/ZnAl-LDH-IL, and Zr, N-ZnO/ZnAl-LDH-IL samples in terms of Kubelka-Munk function vs. wavelength, which

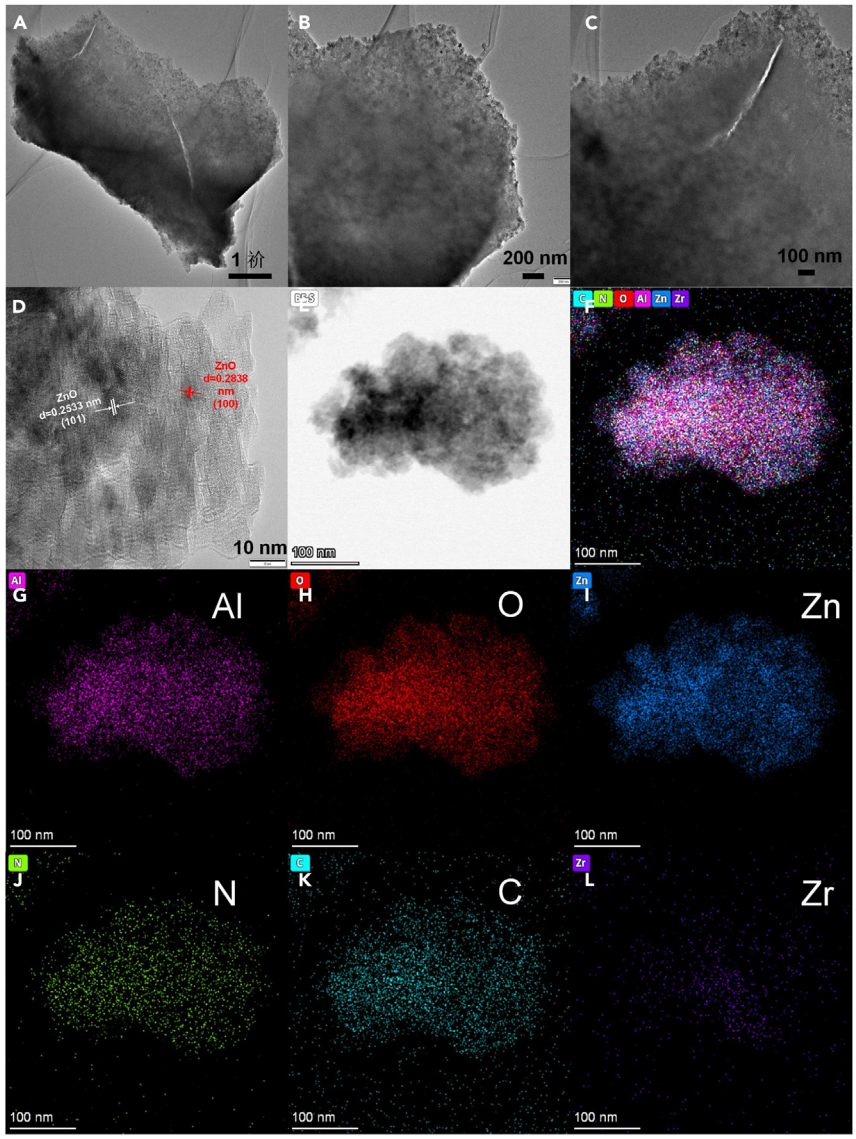

Figure 3. TEM images

(A–D) TEM images of Zr, N-ZnO/ZnAl-LDH-IL composites.

(E and F) Catalyst morphology and element distribution, and corresponding elemental mappings images of Al (G), O (H), Zn (I), N (J), C (K), and Zr (L) of Zr, N-ZnO/ZnAl-LDH-IL composites.

exhibited strong UV light absorption and some visible-light absorption. The absorption range of sample N-ZnAl-LDH-IL was relatively narrow with an absorption edge of about 450 nm, while the samples of N-ZnO/ZnAl-LDH-IL and Zr, N-ZnO/ZnAl-LDH-IL showed an absorption edge of about 560 nm, which could be attributed to the doping of ZnO and Zr.[39,40] From Figure 5B, the optical bandgaps of the samples were also determined according to tauc plots.[34] The forbidden band of the prepared N-ZnAl-LDH-IL material was about 1.83 eV, while the band gap at about 3.42 eV of the N-ZnO/ZnAl-LDH-IL composite was relatively close to that of ZnO reported in the literature, which indicated the successful doping of Zr into N-ZnO/ZnAl-LDH-IL.[40]

The detailed elemental chemical states of N-ZnO/ZnAl-LDH-IL and Zr, N-ZnO/ZnAl-LDH-IL composites were investigated by XPS. Figure 6A provided the survey XPS spectra of the N-ZnO/ZnAl-LDH-IL and Zr, N-ZnO/ZnAl-LDH-IL composites, confirming that the samples were consisted of the elements Zn, O, N, C, Al and the successful introduction of Zr, which was consistent with the element mapping images in Figure 3. Figures 6B–6F represented the high-resolution XPS spectra of Zn 2p, Al 2p, Zr 3d, O 1s and C 1s in the N-ZnO/ZnAl-LDH-IL and Zr, N-ZnO/ZnAl-LDH-IL composites. In Figure 6B, Zn 2p XPS spectra showed two peaks at 1020.71 and 1044.33 eV corresponding to Zn 2p 3/2 and Zn 2p 1/2, with the Zr-doped N-ZnO/ZnAl-LDH-IL composites Zn 2p 3/2 shifting toward higher binding energy, indicating a change in the chemical environment.[22,41] As the binding energy of the elements increased with decreasing electron density, the result suggested that Zn in

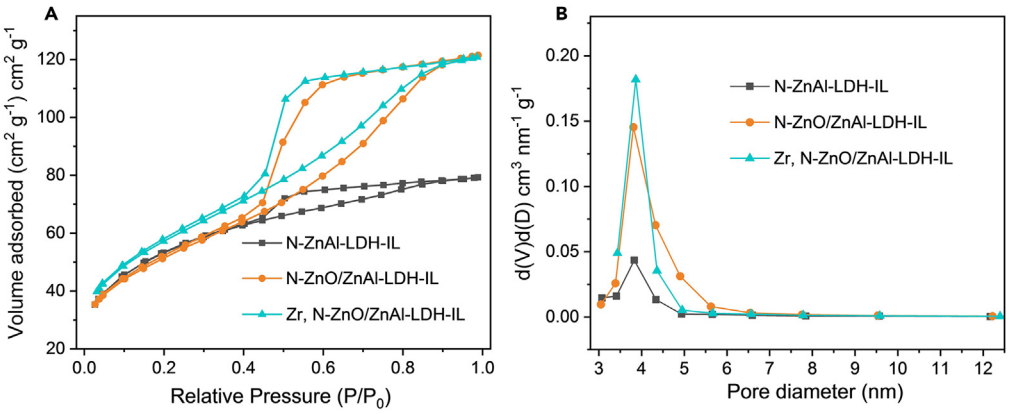

Figure 4. Analysis of specific surface area and pore size of catalysts

(A) N_2 adsorption-desorption isotherms of the N-ZnAl-LDH-IL, N-ZnO/ZnAl-LDH-IL and Zr, N-ZnO/ZnAl-LDH-IL composites.

(B) BJH pore size distribution curves of the N-ZnAl-LDH-IL, N-ZnO/ZnAl-LDH-IL and Zr, N-ZnO/ZnAl-LDH-IL composites.

Zr, N-ZnO/ZnAl-LDH-IL composites had a higher oxidation state compared to N-ZnO/ZnAl-LDH-IL.[42] Figure 6C was the Al 2p spectrum at 73.77 eV, and Figure 6D denoted the Zr 3d XPS spectra of Zr, N-ZnO/ZnAl-LDH-IL composites. It could be fitted into three XPS peaks at 181.30, 182.14 and 183.76 eV, which could be ascribed to the Zr^{3+} 3d 5/2, Zr^{4+} 3d 5/2, and Zr^{3+} 3d 3/2 of Zr, N-ZnO/ZnAl-LDH-IL composites, respectively.[27,34,43] As shown in Figure 6E, the O 1s XPS spectra in the N-ZnO/ZnAl-LDH-IL composites could be fitted into three peaks at 530.2, 531.21, and 532.14 eV. The O1s XPS spectra in the Zr, N-ZnO/ZnAl-LDH-IL composites could be fitted into three peaks at 530.52, 531.05, and 531.92 eV, which corresponded to the lattice oxygen atoms, oxygen atoms neighbor to defects, and oxygen atoms of surface hydroxyl groups.[34,44–46] In Figure 6F, the high-resolution C 1 s XPS spectra of the N-ZnO/ZnAl-LDH-IL composites could be fitted to three peaks centered at 284.8, 286.33, and 288.53 eV, corresponding to C-C/C=C, C-N/C-O, and O-C=O.[47] In contrast, the high-resolution C 1 s XPS spectra of the Zr, N-ZnO/ZnAl-LDH-IL samples was classified as C-C/C=C (284.8 eV), C-N/C=N (285.8 eV), C-N/C-O (286.33 eV) and O-C=O (288.53 eV).[48] Indeed, the element mapping images of Figures 3J and 3K demonstrated similar distributions of C and N on the Zr, N-ZnO/ZnAl-LDH-IL composites, which further corroborated that the doping of Zr affects the form of C and N present on the N-ZnO/ZnAl-LDH-IL samples, with the doping of Zr causing more of the sample to be C allocation to N, which in turn promotes the production of C-N/C =N (285.13 eV).[49]

In Figure 7A, the high-resolution *N* 1 s spectra of N-ZnO/ZnAl-LDH-IL, and Zr, N-ZnO/ZnAl-LDH-IL were divided into five types: pyridinic-N (398.94 eV), Zn-N_x (400.3), pyrrolic-N (401.5 eV), graphitic-N (402.91 eV), and oxidized-N (402.8 eV).[21,33,50,51] The ratios of the different convolutional N 1s bonding types were summarized in Figure 7B. In the N-ZnO/ZnAl-LDH-IL samples, for pyridinic-N, Zn-N_x, pyrrolic-N, graphitic-N, and oxidized-N, 5.48%, 4.46%, 33.28%, 11%, and 45.78% of the total composition, respectively.[22,52] However, after Zr doping, the contents of pyridinic-N, Zn-Nx, and graphitic-N increased to 22.25%, 12.14%, and 19.22%, respectively, and the content of pyrrolic-N and oxidized-N decreased to 12.49% and 33.9%, respectively, with the change in elemental composition, which suggested that the introduction of Zr changed the bonding form of N and C in the samples, even for the small amount of C contained in the samples. The proportions of pyridinic-N and pyrrolic-N in N-doped C materials significantly affected the catalytic performance exhibited by the catalyst, mainly because the form of N present affected the active center, with pyridinic-N (N atoms attached to two carbon atoms) at the edges of the material acting on the adjacent C atoms to give them properties of the base.[21,23]

To investigate this influence of Zr doping on alkalinity and acidity site strength, CO_2-TPD and NH_3-TPD profiles were carried out in Figure 8. As shown in Figure 8A, the desorption peaks of CO_2 appeared at 100°C–200°C (weak basic sites) and 400°C–700°C (strong basic sites), respectively.[53] The weak basic sites were attributed to -OH on the surface of the N-ZnO/ZnAl-LDH-IL composites, while the strong peaks represented the desorption of CO_2, which was chemisorbed on the strong Lewis basic sites.[54] Compared to the sample of N-ZnO/ZnAl-LDH-IL, the Zr, N-ZnO/ZnAl-LDH-IL composites showed weaker desorption peaks at 100°C–200°C, which possibly resulted from the reduced consumption of oxygen-containing groups on the catalyst surface, such as -OH groups, during the Zr doping process.[55] At 400°C–700°C, the Zr, N-ZnO/ZnAl-LDH-IL composites exhibited a significantly stronger CO_2 desorption signal peak than the N-ZnO/ZnAl-LDH-IL samples. Specifically,

Table 1. Physical and chemical l properties of the samples

Samples	Surface area (m^2 g^{-1})	Pore diameter (nm)	Pore volume (cm^3 g^{-1})
N-ZnAl-LDH-IL	192.049	3.828	0.112
N-ZnO/ZnAl-LDH-IL	183.087	3.808	0.175
Zr, N-ZnO/ZnAl-LDH-IL	205.542	3.865	0.173

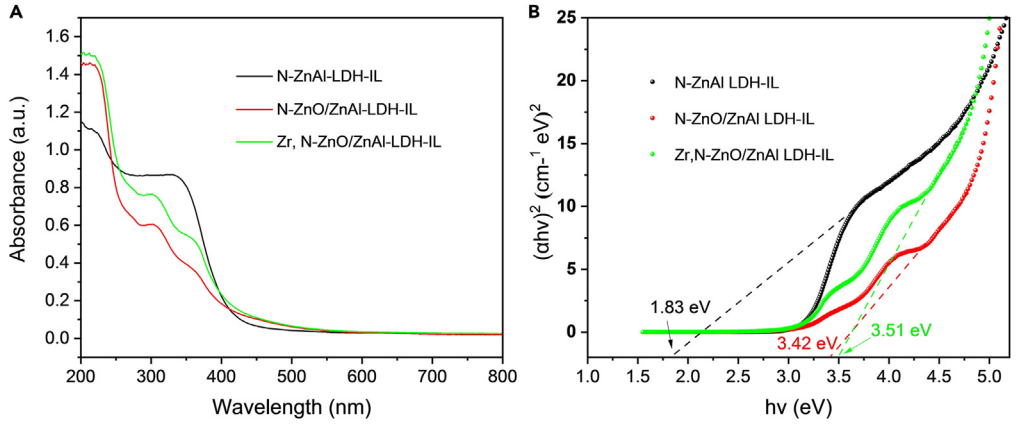

Figure 5. Analysis of photo-absorption property of catalysts

(A) UV-visible diffuse reflection absorption spectra.

(B) The estimated bandgaps of N-ZnAl-LDH-IL, N-ZnO/ZnAl-LDH-IL and Zr, N-ZnO/ZnAl-LDH-IL composites.

the integration yields that the strong basic site of the Zr-doped sample was increased by a factor of 4.16 times. Zr incorporation led to the recombination of N-containing species on N-ZnO/ZnAl-LDH-IL, where the increase in pyridinic-N content caused by Zr incorporation was the main reason why Zr, N-ZnO/ZnAl-LDH-IL composites exhibited more strong basic sites. Figure 8B presented the NH_3-TPD test results of the samples and it could be seen that the signal peaks of the Zr-doped samples at >400°C were obviously shifted to higher temperatures, indicating that the doping of Zr improved the Lewis acidity of the materials. In particular, the N-ZnO/ZnAl-LDH-IL and N-ZnO/ZnAl-LDH-IL composites Zr, N-ZnO and Zr, and the N-ZnAl-LDH-IL composites possessed similar peak area integrals at >400°C, reflecting that the densities of strong Lewis acid sites were essentially the same for both. This indicated that Zr doping made the strong Lewis acid sites on the surface of N-ZnO/ZnAl-LDH-IL composites more acidic without affecting the concentration of strong Lewis acid sites on the surface of the materials.[27,43]

Catalytic performance and possible catalytic mechanism

In order to investigate the influence of the material synthesis environment and the *in situ* generation of ZnO on the properties of N-ZnAl-LDH-IL materials, as well as the influence of the changes in the physical and chemical properties of the material caused by Zr doping on the catalyst performance, the performance of EC prepared directly from CO_2 and EG without the presence of a solvent was chosen as a criterion to evaluate the catalytic performance of the prepared samples. The catalytic performance of each sample was shown in Figure 9, and it is not difficult to find that the yield of N-ZnAl-LDH-IL catalyst for the preparation of EC from CO_2 and EG was 2.7 $mmol_{EC}\ g_{Cat.}^{-1}\ h^{-1}$. The N-ZnO/ZnAl-LDH-IL composite was formed by *in situ* loading of ZnO on the catalyst, and the efficiency of the catalyst for the preparation of EC from CO_2 and EG was increased by 0.75 $mmol_{EC}\ g_{Cat.}^{-1}\ h^{-1}$ per hour. In addition, N-ZnO-IL samples were prepared under the same conditions and the activity of that were tested as a comparison. The results showed that the catalytic performance of the N-ZnO/ZnAl-LDH-IL composite was 4.42 times higher than that of the N-ZnO-IL sample, and 14.4 times higher than N-Al_2O_3-IL samples. The synergistic interaction between N-ZnAl-LDH-IL and N-ZnO-IL effectively facilitated the production of EC, which might because of the homogeneous growth of ZnO on the surface of ZnAl-LDH, allowing a wider contact of ZnO with the feedstock without affecting the catalytic process of the substrate (N-ZnAl-LDH-IL). The catalytic performance of the Zr, N-ZnO/ZnAl-LDH-IL composites without the addition of dehydrating agent was up to 4.76 $mmol_{EC}\ g_{Cat.}^{-1}\ h^{-1}$, which was an improvement of 1.31 $mmol_{EC}\ g_{Cat.}^{-1}\ h^{-1}$ over the N-ZnO/ZnAl-LDH-IL sample. Lewis acid-basic sites activated both CO_2 and EG. The Zr doping changed the composition of active groups on the catalyst surface, exposed more Lewis basic and stronger Lewis acid sites on the catalyst surface and promoting the activation of CO_2 and EG, which might be the main factor in improving the catalyst performance. Besides, a composite catalyst by loading Fe, Cu, Ce, and La on N-ZnO/ZnAl-LDH-IL was attempted to form and the catalytic activity of that was also explored. Figure 9B showed the performance test results with the specific performance parameters 3.78 $mmol_{EC}\ g_{Cat.}^{-1}\ h^{-1}$, 3.93 $mmol_{EC}\ g_{Cat.}^{-1}\ h^{-1}$, 3.59 $mmol_{EC}\ g_{Cat.}^{-1}\ h^{-1}$, and 3.94 $mmol_{EC}\ g_{Cat.}^{-1}\ h^{-1}$.

The effects of reaction temperature, pressure, time, and amount of catalyst used on the catalytic performance were shown in Figure S2. The results showed that the catalytic effect of the catalyst improved with the increase of reaction temperature, CO_2 pressure and reaction time, and the catalytic efficiency increased significantly with the increase of reaction temperature in the range of 110°C–150°C. When the reaction temperature was >150°C, the increase in temperature did not have much effect on the catalytic performance. Similarly, the catalytic efficiency showed an increasing trend with the increase of reaction pressure. When the amount of catalyst used and the catalytic reaction time increased, the catalytic efficiency of the catalyst showed a significant decreasing trend, but the content of product EC in the catalytic system gradually increased. Furthermore, the catalytic performance of the synthesized Zr, N-ZnO/ZnAl-LDH-IL composites was higher than that of most of the reported metal-based catalysts in the catalytic CO_2 and alcohol production of carbonates (Table S1).

In related reports, the catalytic mechanism for the direct preparation of carbonate esters from CO_2 and alcohols was considered to have multiple pathways, with both Lewis acidic and basic sites activating CO_2 and alcohols (Scheme 1). Thus, Lewis acidic-basic synergistic catalysis

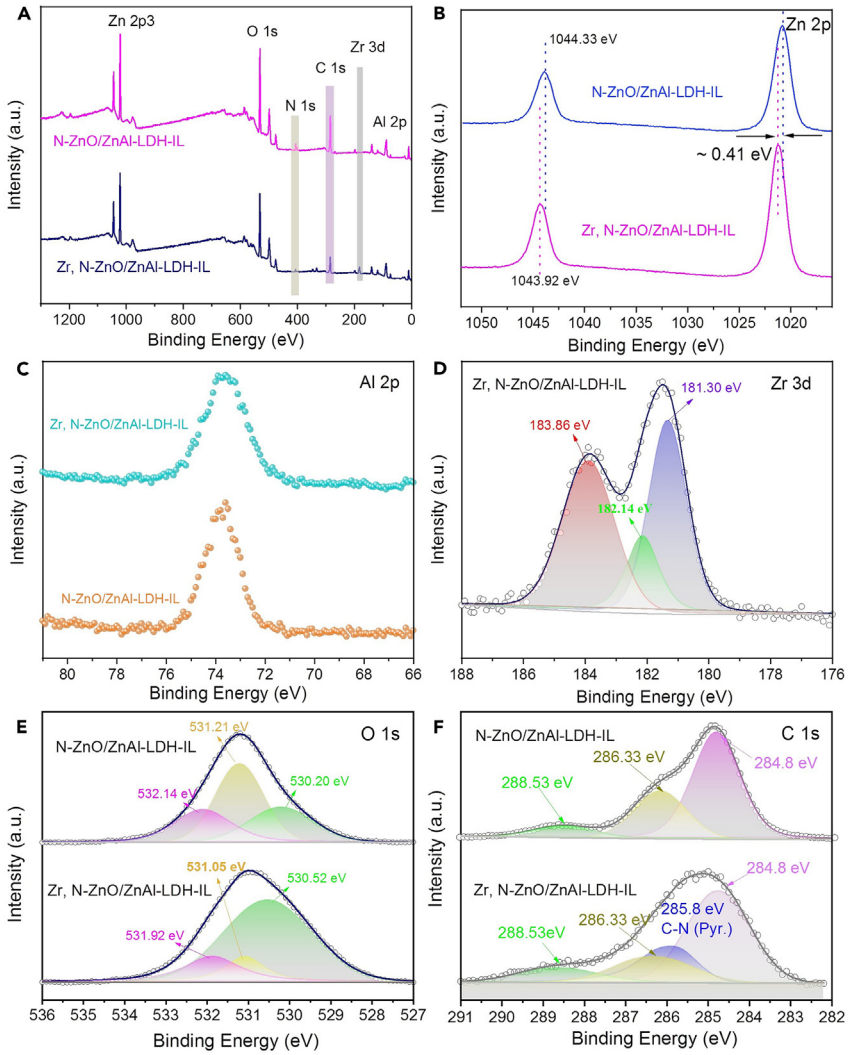

Figure 6. Analysis of XPS spectra

(A) The survey XPS spectra of N-ZnO/ZnAl-LDH-IL, and Zr, N-ZnO/ZnAl-LDH-IL samples.
(B) Zn 2p XPS spectra of N-ZnO/ZnAl-LDH-IL, and Zr, N-ZnO/ZnAl-LDH-IL samples.
(C) Al 2p XPS spectra of N-ZnO/ZnAl-LDH-IL, and Zr, N-ZnO/ZnAl-LDH-IL samples.
(D) Zr 3days XPS spectra of N-ZnO/ZnAl-LDH-IL, and Zr, N-ZnO/ZnAl-LDH-IL samples.
(E) O 1 s XPS spectra of N-ZnO/ZnAl-LDH-IL, and Zr, N-ZnO/ZnAl-LDH-IL samples.
(F) C 1s XPS spectra of N-ZnO/ZnAl-LDH-IL, and Zr, N-ZnO/ZnAl-LDH-IL samples.

was regarded as one of the possible pathways. Combined with the analysis of the characterization and activity test results, the direct synthesis of EC from CO_2 and EG $(CH_2OH)_2$ in this study was attributed to the synergistic effect of the Lewis acidic-basic sites on the catalyst surface. The oxygen atom in $(CH_2OH)_2$ was adsorbed on the acidic sites of the catalyst and the H atom attached to the oxygen atom bond the basic site on the catalyst surface to form the adsorbed states $-OCH_2CH_2OH$ and -H. The basic sites on the catalyst surface provided electrons to the C atoms in the CO_2 molecules adsorbed on that, and the activated O-C-O bond the adsorbed state of $-OCH_2CH_2OH$. Immediately afterward, the Lewis basic site on the catalyst surface and the oxygen atom at the O-C-O terminus acted together on $-OCH_2CH_2OH$, transporting electrons to the C atom and -OH attached to the terminus, facilitating the removal of the -OH group and eventually closing the ring to form EC. Meanwhile, -OH combined with the adsorbed -H to form the by-product H_2O.

Conclusions

In methanol and ILs solutions, Zr, N-ZnO/ZnAl-LDH-IL composites were successfully synthesized by *in-situ* doping methods for enhancing the performance of direct EC preparation with CO_2 and EG. After introducing Zr into the N-ZnO/ZnAl-LDH-IL composites, the material still maintained a high specific surface area of 205.542 $m^2\ g^{-1}$. Moreover, the doping of Zr effectively induced the changes in the reactive groups on the

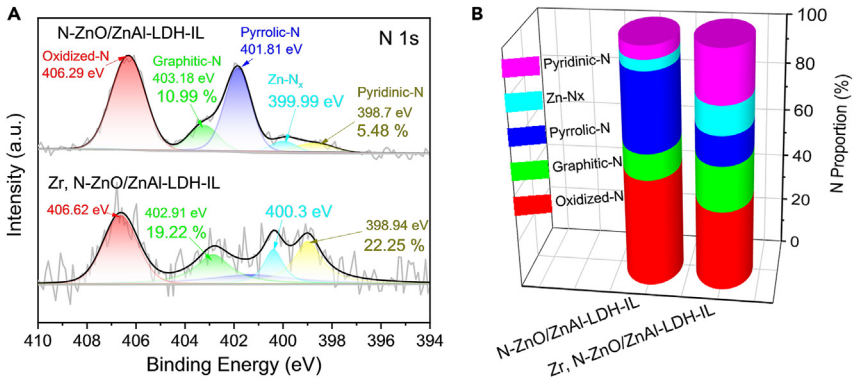

Figure 7. Analysis of N 1s XPS spectra

(A) XPS spectra of the prepared samples: *N* 1 s.

(B) Proportion of *N* 1 s bonding types (%).

catalyst surface, prompting the formation of more pyridinic-N, which led to an increase in the number of strong basic sites on the catalyst surface. The prepared Zr, N-ZnO/ZnAl-LDH-IL composites exhibited about 4.16 times more strong Lewis basic sites than the ZnO/ZnAl-LDH-IL composites, and showed the best performance in catalytic CO_2 and EG preparation of EC at about 4.76 $mmol_{EC}\ g_{Cat.}^{-1}\ h^{-1}$, which was 4.42 times higher than that of the N-ZnO-IL sample, and 14.4 times higher than N-Al_2O_3-IL sample. Besides, the experimental results also indicated that the doping of La, Ce, Fe, and Cu also enhanced the performance of the materials in the direct synthesis of EC from CO_2 and EG. Meanwhile, another efficient strategy to fabricate metal and nonmetal co-doped, high specific surface area, and surface groups tunable layered double hydroxides for CO_2 capture and utilization was proposed.

Limitations of the study

In our work, we obtained ZnAl-LDH substrates in methanol-ionic liquid systems and explored the effect of surface physical properties on the synthesis of EC from CO_2 and EG. The synthesis process was carried out in methanol-ionic liquid in order to obtain ZnAl-LDH-IL with *in-situ* doping with ZnO, and if the synthesis was carried out in water a ZnAl-LDH with better crystallinity could be obtained. Compared to the conventional ZnAl-LDH materials, the synthesis of ZnAl-LDH-IL omits the crystallization and precipitation step in order to be easier to modify, but the disadvantage of low crystallinity is exposed. Furthermore, we still need to investigate whether different types of LDH materials can be formed in methanol-ionic liquid systems, the modulation of their surface physical properties and the effect on the activity, which will be our future research direction.

STAR★METHODS

Detailed methods are provided in the online version of this paper and include the following:

- KEY RESOURCES TABLE
- RESOURCE AVAILABILITY

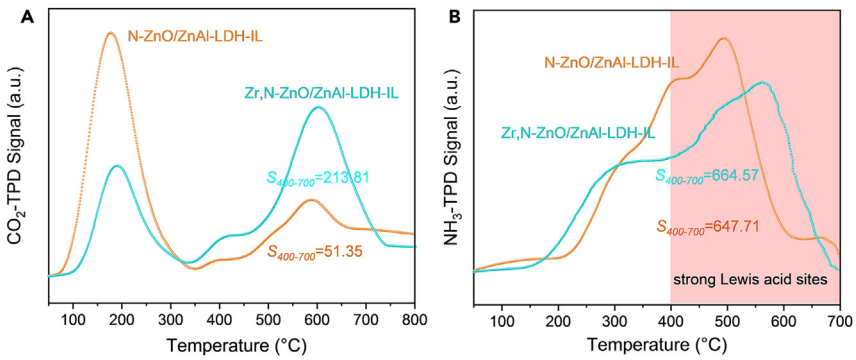

Figure 8. TPD analysis curves of N-ZnO/ZnAl-LDH-IL, and Zr, N-ZnO/ZnAl-LDH-IL samples

(A) CO_2-TPD profiles of N-ZnO/ZnAl-LDH-IL, and Zr, N-ZnO/ZnAl-LDH-IL samples.

(B) NH_3-TPD profiles of N-ZnO/ZnAl-LDH-IL, and Zr, N-ZnO/ZnAl-LDH-IL samples.

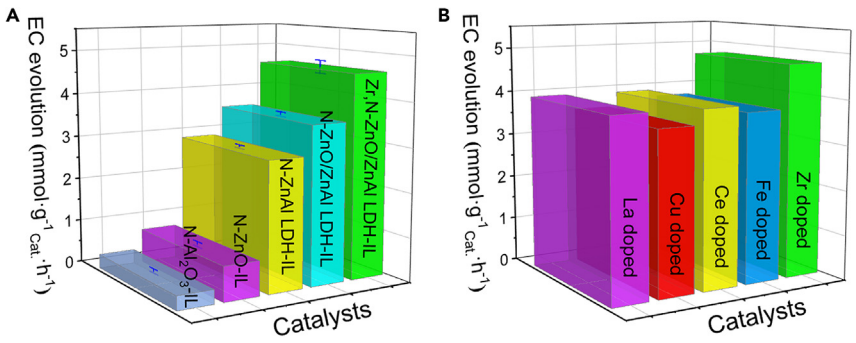

Figure 9. Catalytic performance of all catalysts

(A) Catalytic performances of N-ZnO-IL, N-ZnAl-LDH-IL, N-ZnO/ZnAl-LDH-IL, and Zr, N-ZnO/ZnAl-LDH-IL composites for the direct EC synthesis from CO_2 and EG at 130°C and 3 MPa, and the data of Zr, N-ZnO/ZnAl-LDH-IL composites is represented as mean 4.76 ± 0.15 $mmol_{EC}\ g_{Cat.}^{-1}\ h^{-1}$.

(B) Catalytic performance of N-ZnO/ZnAl-LDH-IL composites loaded with different metals under the same catalytic conditions.

SUPPLEMENTAL INFORMATION

Supplemental information can be found online at https://doi.org/10.1016/j.isci.2024.109714.

ACKNOWLEDGMENTS

This research was funded by the National Natural Science Foundation of China (No. 22178356, No. 21890763, and No. 22078329), the Clean Combustion and Low-carbon Utilization of Coal, Strategic Priority Research Program of the Chinese Academy of Sciences, grant No. XDA29030202, the Key-Area Research and Development Program of Guangdong Province (No.2020B0101370002).

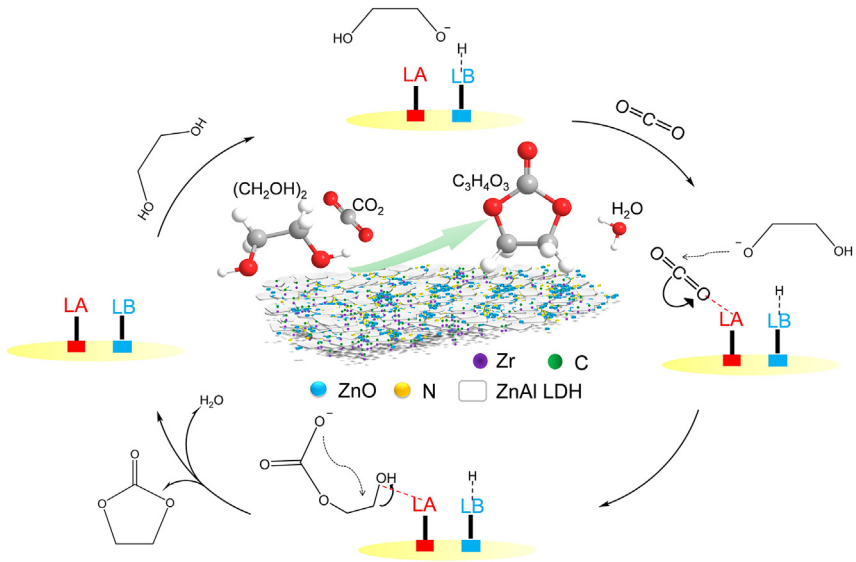

Scheme 1. Possible mechanism for synthetizing EC from EG and CO_2 catalyzed by Zr, N-ZnO/ZnAl-LDH-IL composites

AUTHOR CONTRIBUTIONS

J.H.: conceptualization, methodology, validation, formal analysis, investigation, data curation, writing-original draft, writing-review and editing and visualization. **J.W.:** data curation, formal analysis and resources. **H.D.:** data curation and validation. **L.D.:** conceptualization, methodology, writing-review and editing, funding acquisition, project administration. **S.C.:** data curation and validation. **J.Z.:** conceptualization, methodology, writing-review and editing. **X.Z.:** conceptualization, methodology and writing-review and editing.

DECLARATION OF INTERESTS

The authors declare no known competing interests.

Received: November 21, 2023
Revised: January 16, 2024
Accepted: April 7, 2024
Published: April 9, 2024

REFERENCES

1. Yu, W., Gao, M., Rim, G., Feric, T.G., Rivers, M.L., Alahmed, A., Jamal, A., and Alissa Park, A.-H. (2023). Novel in-capsule synthesis of metal-organic framework for innovative carbon dioxide capture system. Green Energy Environ. *8*, 767–774. https://doi.org/10.1016/j.gee.2021.08.002.
2. Li, Y., Li, F., Laaksonen, A., Wang, C., Cobden, P., Boden, P., Liu, Y., Zhang, X., and Ji, X. (2023). Electrochemical CO_2 reduction with ionic liquids: review and evaluation. Ind. Chem. Mater. *1*, 410–430. https://doi.org/10.1039/d2im00055e.
3. Shao, B., Zhang, Y., Sun, Z., Li, J., Gao, Z., Xie, Z., Hu, J., and Liu, H. (2022). CO_2 capture and in-situ conversion: recent progresses and perspectives. Green Chem. Eng. *3*, 189–198. https://doi.org/10.1016/j.gce.2021.11.009.
4. Xu, G., Shi, M., Ning, H., Zheng, L., Tu, Z., Zhang, X., Hu, X., and Wu, Y. (2023). Constructing stable protic ionic liquids with cuprous site and long alkyl chain for highly efficient separation of propylene and propane. Separ. Purif. Technol. *323*, 124403. https://doi.org/10.1016/j.seppur.2023.124403.
5. Hu, J., Yu, L., Deng, J., Wang, Y., Cheng, K., Ma, C., Zhang, Q., Wen, W., Yu, S., Pan, Y., et al. (2021). Sulfur vacancy-rich MoS_2 as a catalyst for the hydrogenation of CO_2 to methanol. Nat. Catal. *4*, 242–250. https://doi.org/10.1038/s41929-021-00584-3.
6. Zhang, F., Li, Y.-H., Qi, M.-Y., Yamada, Y.M., Anpo, M., Tang, Z.-R., and Xu, Y.-J. (2021). Photothermal catalytic CO_2 reduction over nanomaterials. Chem Catal. *1*, 272–297. https://doi.org/10.1016/j.checat.2021.01.003.
7. Ding, Y., Dong, Y., Ma, M., Luo, L., Wang, X., Fang, B., Li, Y., Liu, L., and Ren, F. (2023). CO_2 electrocatalytic reduction to ethylene and its application outlook in food science. iScience *26*, 108434. https://doi.org/10.1016/j.isci.2023.108434.
8. Liu, M., Ma, C., Cheng, X., Gao, K., Zhang, G., Wang, D., and Liu, F. (2023). New insight into multiple hydrogen-bond networks of functional organosilicas system for collaborative transformation of CO_2 under mild conditions. Separ. Purif. Technol. *317*, 123937. https://doi.org/10.1016/j.seppur.2023.123937.
9. Jeon, S.S., Kang, P.W., Klingenhof, M., Lee, H., Dionigi, F., and Strasser, P. (2023). Active Surface Area and Intrinsic Catalytic Oxygen Evolution Reactivity of NiFe LDH at Reactive Electrode Potentials Using Capacitances. ACS Catal. *13*, 1186–1196. https://doi.org/10.1021/acscatal.2c04452.
10. Honda, M., Tamura, M., Nakao, K., Suzuki, K., Nakagawa, Y., and Tomishige, K. (2014). Direct Cyclic Carbonate Synthesis from CO_2 and Diol over Carboxylation/Hydration Cascade Catalyst of CeO_2 with 2-Cyanopyridine. ACS Catal. *4*, 1893–1896. https://doi.org/10.1021/cs500301d.
11. Hu, J., Ma, W., Liu, Q., Geng, J., Wu, Y., and Hu, X. (2023). Reaction and separation system for CO_2 hydrogenation to formic acid catalyzed by iridium immobilized on solid phosphines under base-free condition. iScience *26*, 106672. https://doi.org/10.1016/j.isci.2023.106672.
12. Terrade, F.G., Lutz, M., van der Vlugt, J.I., and Reek, J.N.H. (2013). Synthesis, Coordination Chemistry, and Cooperative Activation of H_2 with Ruthenium Complexes of Proton-Responsive METAMORPhos Ligands. Eur. J. Inorg. Chem. *2014*, 1826–1835. https://doi.org/10.1002/ejic.201301215.
13. Huang, S.-Y., Liu, S.-G., Li, J.-P., Zhao, N., Wei, W., and Sun, Y.-H. (2007). Synthesis of cyclic carbonate from carbon dioxide and diols over metal acetates. J. Fuel Chem. Technol. *35*, 701–705. https://doi.org/10.1016/s1872-5813(08)60005-5.
14. Bobbink, F.D., Gruszka, W., Hulla, M., Das, S., and Dyson, P.J. (2016). Synthesis of cyclic carbonates from diols and CO_2 catalyzed by carbenes. Chem. Commun. *52*, 10787–10790. https://doi.org/10.1039/c6cc05730f.
15. Hu, J., Yu, C., Li, C., Lan, S., Zeng, L., and Zhu, M. (2022). Thickness-dependent piezo-photo-responsive behavior of ZnAl-layered double hydroxide for wastewater remediation. Nano Energy *101*, 107583. https://doi.org/10.1016/j.nanoen.2022.107583.
16. Li, M., Li, P., Zhang, L., Chen, M., Tang, J., Qin, C., Ling Jie Lee, S., and Lin, S. (2022). Facile fabrication of ZnO decorated ZnFe-layered double hydroxides @ biochar nanocomposites for synergistic photodegradation of tetracycline under visible light. Chem. Eng. J. *434*, 134772. https://doi.org/10.1016/j.cej.2022.134772.
17. Qiu, C., Cai, F., Wang, Y., Liu, Y., Wang, Q., and Zhao, C. (2020). 2-Methylimidazole directed ambient synthesis of zinc-cobalt LDH nanosheets for efficient oxygen evolution reaction. J. Colloid Interface Sci. *565*, 351–359. https://doi.org/10.1016/j.jcis.2019.12.070.
18. Jiang, Y.-F., Jiang, N., Liang, K., Yuan, C.-Z., Fang, X.-X., and Xu, A.-W. (2019). A simple and general route to prepare functional mesoporous double-metal oxy(hydroxide). J. Mater. Chem. A Mater. *7*, 7932–7938. https://doi.org/10.1039/c8ta10719j.
19. Mishra, K., Devi, N., Siwal, S.S., Zhang, Q., Alsanie, W.F., Scarpa, F., and Thakur, V.K. (2022). Ionic Liquid-Based Polymer Nanocomposites for Sensors, Energy, Biomedicine, and Environmental Applications: Roadmap to the Future. Adv. Sci. *9*, e2202187. https://doi.org/10.1002/advs.202202187.
20. Nolan, N.T., Synnott, D.W., Seery, M.K., Hinder, S.J., Van Wassenhoven, A., and Pillai, S.C. (2012). Effect of N-doping on the photocatalytic activity of sol–gel TiO_2. J. Hazard Mater. *211–212*, 88–94. https://doi.org/10.1016/j.jhazmat.2011.08.074.
21. Ohtsubo, N., Gohda, S., Gotoh, K., Sato, S., and Yamada, Y. (2023). Bottom-up synthesis of pyridinic nitrogen-containing carbon materials with C–H groups next to pyridinic nitrogen from two-ring aromatics. Carbon *207*, 270–291. https://doi.org/10.1016/j.carbon.2023.02.019.
22. Xie, C., Lin, L., Huang, L., Wang, Z., Jiang, Z., Zhang, Z., and Han, B. (2021). Zn-Nx sites on N-doped carbon for aerobic oxidative cleavage and esterification of C(CO)-C bonds. Nat. Commun. *12*, 4823. https://doi.org/10.1038/s41467-021-25118-0.
23. Guo, D., Shibuya, R., Akiba, C., Saji, S., Kondo, T., and Nakamura, J. (2016). Active sites of nitrogen-doped carbon materials for oxygen reduction reaction clarified using model catalysts. Science *351*, 361–365. https://doi.org/10.1126/science.aad0832.
24. Guo, C., Shen, S., Li, M., Wang, Y., Li, J., Xing, Y., Wang, C., and Pan, H. (2021). Rapid *in situ* synthesis of MgAl-LDH on η-Al2O3 for efficient hydrolysis of urea in wastewater. J. Catal. *395*, 54–62. https://doi.org/10.1016/j.jcat.2020.12.024.
25. Keyikoglu, R., Khataee, A., Lin, H., and Orooji, Y. (2022). Vanadium (V)-doped ZnFe layered double hydroxide for enhanced sonocatalytic degradation of pymetrozine. Chem. Eng. J. *434*, 134730. https://doi.org/10.1016/j.cej.2022.134730.
26. Li, C., Sun, Y., Hess, F., Djerdj, I., Sann, J., Voepel, P., Cop, P., Guo, Y., Smarsly, B.M., and Over, H. (2018). Catalytic HCl oxidation

reaction: Stabilizing effect of Zr-doping on CeO2 nano-rods. Appl. Catal. B Environ. *239*, 628–635. https://doi.org/10.1016/j.apcatb.2018.08.047.

27. Zhang, X., Li, M., Cui, X., Niu, X., and Zhu, Y. (2023). Enhancing catalytic activity for toluene and acetone oxidation over ZraCo1-aOx catalysts by doping Zr to improve the oxygen activation capacity due to formation of Zr-O-Co bonds. Chem. Eng. J. *465*, 142857. https://doi.org/10.1016/j.cej.2023.142857.
28. Byzynski, G., Melo, C., Volanti, D.P., Ferrer, M.M., Gouveia, A.F., Ribeiro, C., Andrés, J., and Longo, E. (2017). The interplay between morphology and photocatalytic activity in ZnO and N-doped ZnO crystals. Mater. Des. *120*, 363–375. https://doi.org/10.1016/j.matdes.2017.02.020.
29. Singh, S., Sharma, R., and Mehta, B.R. (2017). Enhanced surface area, high Zn interstitial defects and band gap reduction in N-doped ZnO nanosheets coupled with $BiVO_4$ leads to improved photocatalytic performance. Appl. Surf. Sci. *411*, 321–330. https://doi.org/10.1016/j.apsusc.2017.03.189.
30. Li, X., Yu, Z., Shao, L., Zeng, H., Liu, Y., and Feng, X. (2020). A novel strategy to construct a visible-light-driven Z-scheme (ZnAl-LDH with active phase/g-C_3N_4) heterojunction catalyst via polydopamine bridge (a similar "bridge" structure). J. Hazard Mater. *386*, 121650. https://doi.org/10.1016/j.jhazmat.2019.121650.
31. Zhao, J., Shi, R., Waterhouse, G.I., and Zhang, T. (2022). Selective photothermal CO_2 reduction to CO, CH_4, alkanes, alkenes over bimetallic alloy catalysts derived from layered double hydroxide nanosheets. Nano Energy *102*, 107650. https://doi.org/10.1016/j.nanoen.2022.107650.
32. Hameed, A., Batool, M., Liu, Z., Nadeem, M.A., and Jin, R. (2022). Layered Double Hydroxide-Derived Nanomaterials for Efficient Electrocatalytic Water Splitting: Recent Progress and Future Perspective. ACS Energy Lett. *7*, 3311–3328. https://doi.org/10.1021/acsenergylett.2c01362.
33. Li, F., Sun, S.-K., Chen, Y., Naka, T., Hashishin, T., Maruyama, J., and Abe, H. (2022). Bottom-up synthesis of 2D layered high-entropy transition metal hydroxides. Nanoscale Adv. *4*, 2468–2478. https://doi.org/10.1039/d1na00871d.
34. Huang, J., Liu, J., Tian, L., Li, X., Ma, X., Yu, X., Guo, Q., and Zhao, J. (2021). Ultrathin carbon-coated Zr^{3+}-ZrO_2 nanostructures for efficient visible light photocatalytic antibiotic elimination. Chem. Eng. J. *412*, 128621. https://doi.org/10.1016/j.cej.2021.128621.
35. Li, X., Chen, H., Zhang, L., Wang, Z., Wu, S., and Ma, J. (2023). The interface design and properties enhancement of ZnO/cellulose composites: Branching fiber network to guide the assembly of ZnO flower. J. Colloid Interface Sci. *641*, 539–552. https://doi.org/10.1016/j.jcis.2023.03.096.
36. Huang, J., Liu, S., Long, W., Wang, Q., Yu, X., and Li, S. (2021). Highly enhanced photodegradation of emerging pollutants by Ag/AgCl/Ta_2O_{5-x} mesocrystals. Separ. Purif. Technol. *279*, 119733. https://doi.org/10.1016/j.seppur.2021.119733.
37. Jing, H., Ji, L., Li, Z., Wang, Z., Li, R., and Ju, K. (2023). Zn/Fe bimetallic modified Spartina alterniflora-derived biochar heterostructure with superior catalytic performance for the degradation of malachite green. Biochar *5*, 29. https://doi.org/10.1007/s42773-023-00227-9.
38. Wei, F., Liu, L., Wang, C., Wu, X., and Du, Y. (2023). Cu(Mn)MgAl mixed oxides with enhanced performance for simultaneous removal of NO_x and toluene: Insight into the better collaboration of CuO and MnO_x via layered double hydroxides (LDHs) precursor template. Chem. Eng. J. *462*, 142150. https://doi.org/10.1016/j.cej.2023.142150.
39. Long, C., Han, J., Guo, J., Yang, C., Liu, S., and Tang, Z. (2021). Operando toolbox for heterogeneous interface in electrocatalysis. Chem Catal. *1*, 509–522. https://doi.org/10.1016/j.checat.2021.07.012.
40. Li, Z., Pan, X., and Yi, Z. (2019). Photocatalytic oxidation of methane over CuO-decorated ZnO nanocatalysts. J. Mater. Chem. A Mater. *7*, 469–475. https://doi.org/10.1039/c8ta09592b.
41. Ou, R., Zeng, Z., Ning, X., Zeng, B., and Wu, C. (2022). Improved photocatalytic performance of N-doped ZnO/graphene/ZnO sandwich composites. Appl. Surf. Sci. *577*, 151856. https://doi.org/10.1016/j.apsusc.2021.151856.
42. Huang, Z., Zhou, Q., Wang, J., and Yu, Y. (2022). Fermi-level-tuned MOF-derived N-ZnO@NC for photocatalysis: A key role of pyridine-N-Zn bond. J. Mater. Sci. Technol. *112*, 68–76. https://doi.org/10.1016/j.jmst.2021.10.017.
43. Wang, W., Song, S., Wang, P., He, M., Fang, Z., Yuan, X., Li, H., Li, C., Wang, X., Wei, Y., et al. (2023). Chemical Bonding of g-C_3N_4/UiO-66(Zr/Ce) from Zr and Ce Single Atoms for Efficient Photocatalytic Reduction of CO_2 under Visible Light. ACS Catal. *13*, 4597–4610. https://doi.org/10.1021/acscatal.2c06255.
44. Li, X., Wang, X., Ding, J., Ma, M., Yuan, S., Yang, Q., Wang, Z., Peng, Y., Sun, C., Zhou, H., et al. (2023). Engineering Active Surface Oxygen Sites of Cubic Perovskite Cobalt Oxides toward Catalytic Oxidation Reactions. ACS Catal. *13*, 6338–6350. https://doi.org/10.1021/acscatal.3c00139.
45. Zhang, C., Li, T., Xue, B., Wu, X., Li, L., Guo, Y., and Zhang, L. (2023). Synergistic modification of Ni-rich full concentration gradient materials with enhanced thermal stability. Chem. Eng. J. *451*, 138518. https://doi.org/10.1016/j.cej.2022.138518.
46. Zhu, C., Lu, L., Xu, J., Song, S., Fang, Q., Liu, R., Shen, Y., Zhao, J., Dong, W., and Shen, Y. (2023). Metal monovacancy-induced spin polarization for simultaneous energy recovery and wastewater purification. Chem. Eng. J. *451*, 138537. https://doi.org/10.1016/j.cej.2022.138537.
47. Wang, X., Liu, T., Li, H., Han, C., Su, P., Ta, N., Jiang, S.P., Kong, B., Liu, J., and Huang, Z. (2023). Balancing Mass Transfer and Active Sites to Improve Electrocatalytic Oxygen Reduction by B,N Codoped C Nanoreactors. Nano Lett. *23*, 4699–4707. https://doi.org/10.1021/acs.nanolett.3c00202.
48. Song, T., Zhang, X., Xie, C., and Yang, P. (2023). N-doped carbon nanotubes enhanced charge transport between Ni nanoparticles and g-C_3N_4 nanosheets for photocatalytic H_2 generation and 4-nitrophenol removal. Carbon *210*, 118052. https://doi.org/10.1016/j.carbon.2023.118052.
49. Wang, J., Zhang, J., Hu, Y., Jiang, H., and Li, C. (2022). Activating multisite high-entropy alloy nanocrystals via enriching M-pyridinic N-C bonds for superior electrocatalytic hydrogen evolution. Sci. Bull. *67*, 1890–1897. https://doi.org/10.1016/j.scib.2022.08.022.
50. Qu, Y., Zhang, W., Guang, B., Xiao, Y., Liu, X., Zhai, C., and Liu, Y. (2022). Poly(ionic liquids) derived N, S co-doped carbon nanorod from *in situ* and template-free method as an efficient metal-free bifunctional electrocatalysts for direct methanol fuel cells. J. Alloys Compd. *912*, 165261. https://doi.org/10.1016/j.jallcom.2022.165261.
51. Pei, Y., Quan, Y., Wang, X., Zhao, J., Shi, R., Li, Z., and Ren, J. (2022). Surface reconstruction induced highly efficient N-doped carbon nanosheet supported copper cluster catalysts for dimethyl carbonate synthesis. Appl. Catal. B Environ. *300*, 120718. https://doi.org/10.1016/j.apcatb.2021.120718.
52. Xiong, N., Li, Y., and Zeng, R. (2023). Merging Photoinduced Iron-Catalyzed Decarboxylation with Copper Catalysis for C-N and C-C Couplings. ACS Catal. *13*, 1678–1685. https://doi.org/10.1021/acscatal.2c05293.
53. Gao, X., Wang, Z., Huang, Q., Jiang, M., Askari, S., Dewangan, N., and Kawi, S. (2022). State-of-art modifications of heterogeneous catalysts for CO_2 methanation – Active sites, surface basicity and oxygen defects. Catal. Today *402*, 88–103. https://doi.org/10.1016/j.cattod.2022.03.017.
54. Zhang, T., Wang, W., Gu, F., Xu, W., Zhang, J., Li, Z., Zhu, T., Xu, G., Zhong, Z., and Su, F. (2022). Enhancing the low-temperature CO_2 methanation over Ni/La-CeO_2 catalyst: The effects of surface oxygen vacancy and basic site on the catalytic performance. Appl. Catal. B Environ. *312*, 121385. https://doi.org/10.1016/j.apcatb.2022.121385.
55. Xu, X., Cui, Y., Chen, T., Jiang, K., Wang, J., Xiao, Y., Yang, X., Zhu, J., Chen, H., and Ding, X. (2023). Dual-Site Synergetic Photochemical Activation of Chlorinated Phenols Triggered by Surface Hydroxyls of Photocatalysts under Visible Light. ACS Catal. *13*, 4700–4710. https://doi.org/10.1021/acscatal.3c00189.

STAR★METHODS

KEY RESOURCES TABLE

REAGENT or RESOURCE	SOURCE	IDENTIFIER
Chemicals, peptides, and recombinant proteins		
$Zn(NO_3)_2 \cdot 6H_2O$	Sino-pharm Chemical Reagent Co. Ltd.	10196-18-6
$Al(NO_3)_3 \cdot 9H_2O$	Xilong Scientific Co., Ltd.	7784-27-2
$La(NO_3)_3 \cdot 6H_2O$	Macklin Bio-Chemical Technology Co., Ltd.	10277-43-7
$Cu(NO_3)_2 \cdot 3H_2O$	Macklin Bio-Chemical Technology Co., Ltd.	13778-31-9
$Fe(NO_3)_3 \cdot 9H_2O$	Shanghai Aladdin Bio-Chem Technology Co., Ltd.	7782-61-8
$Ce(NO_3)_3 \cdot 6H_2O$	Shanghai Aladdin Bio-Chem Technology Co., Ltd.	10294-41-4
$ZrO_4C_{16}H_{36}$	Shanghai Aladdin Bio-Chem Technology Co., Ltd.	1071-76-7
$(CH_2OH)_2$	Macklin Bio-Chemical Technology Co., Ltd.	107-21-1
$C_8H_{21}NO$	Shanghai Aladdin Bio-Chem Technology Co., Ltd.	77-98-5 (methanol)
CH_3OH	Shanghai Aladdin Bio-Chem Technology Co., Ltd.	67-56-1

RESOURCE AVAILABILITY

Lead contact

Further information and requests for resources should be directed to and will be fulfilled by the lead contact, Pro. Li Dong (ldong@ipe.ac.cn).

Materials availability

This study did not generate new unique reagents. All the reagents in this work were commercially available and directly used without further purification.

Data and code availability

- Data reported in this paper will be shared by the lead contacts upon reasonable request.
- This study does not report any original code.
- Any additional information required to reanalyze the data reported in this paper is available from the lead contacts upon reasonable request.

EXPERIMENTAL MODEL AND STUDY PARTICIPANT DETAILS

For all the experiments, both catalyst synthesis and characterization tests were carried out at ambient conditions at Institute of Process Engineering, Chinese Academy of Sciences. All the experiments involve no laboratory animals.

METHOD DETAILS

Synthesis of N-ZnO/ZnAl-LDH-IL

Unlike traditional synthesis methods, this method uses alkaline ionic liquids instead of NaOH or urea, so all LDH material synthesis processes do not involve urea and NaOH. N-ZnO/ZnAl-LDH-IL composites were first prepared in the ionic liquid/methanol system by solvothermal strategy. In a typical procedure, 1.79 g $Zn(NO_3)_2 \cdot 6H_2O$ and 0.75 g $Al(NO_3)_3 \cdot 9H_2O$ were added into 30 mL of methanol in a beaker with continuous stirring, and another 9 mL of 25 wt.% tetraethyl ammonium hydroxide methanol solution was added into the above mixture with constant stirring and then stirred at room temperature for 30 min. The resulting precursor N-doped ZnAl-LDH-IL was centrifuged and washed twice with methanol. Afterwards, the precursor was redisposed in 40 mL of methanol, mixed well and transferred to a teflon-lined stainless steel autoclave with a liner capacity of 100 mL. After that, the reactions were carried out at 130°C for 6 h. It is worth noting that when the solvent does not contain an ionic liquid, a solid catalyst cannot be obtained under the same conditions.

Synthesis of metals, N-ZnO/ZnAl-LDH-IL

Similar procedures prepared the Zr, N-ZnO/ZnAl-LDH-IL composites. The difference is that zirconium (IV) butoxide solution was added at the same time as 9 mL of 25 wt. % tetraethyl ammonium hydroxide methanol solution. In addition, we have designed different kinds of

metal-doped samples, and these four samples doped with Ce, Cu, Fe and La denoted as Ce, N-ZnO/ZnAl-LDH-IL; Cu, N-ZnO/ZnAl-LDH-IL; Fe, N-ZnO/ZnAl-LDH-IL, and La, N-ZnO/ZnAl-LDH-IL.

Characterizations

The crystal structure and properties of the samples were obtained from an x-ray diffract meter (SmartLab-9kW, Japan) in 2θ regions of 5-90°. The specific morphology and microscopic morphological structure of the samples were observed on a transmission electron microscope (TEM) (JEOL JEM-2100F) at 200 kV. Information on the surface area and pore size distribution of the sample is obtained on the Quanta chrome Auto sorb-iQ-MP-C. Fourier transforms infrared spectra of the prepared samples were measured on a Fourier-transform infrared spectrometer (Nicolet 380, Thermo Electron Corporation). NH_3 temperature-programmed desorption (NH_3-TPD) and CO_2 temperature-programmed desorption (CO_2-TPD) from prepared samples measured by chemisorption analyzer (Micrometrics Instruments Corp, America). The chemical composition and state of the prepared samples were determined by electron spectrometry (XPS) (ESCALAB 250 Xi, Thermo Fisher Scientific) using the C1s peak (284.8 eV) as a reference.

Evaluation of the prepared catalysts

The catalytic performance of the prepared samples was tested in a micro-reactor (YZPR-25, Yanzheng Shanghai Experimental Instrument Co., Ltd, China.). The efficiency of EC preparation from EG and CO_2 as a catalyst performance evaluation criterion. In a typical procedure, 0.1 g of the prepared Zr, N-ZnO/ZnAl-LDH-IL composites were added into a 35 mL reactor containing 100 mmol of EG at room temperature then start to warm up. When the temperature was raised to 150°C, 3 MPa of CO_2 was passed through the reaction for 1 h. At the end of the catalytic reaction, the EC content of the reaction solution was tested by gas chromatography, where biphenyl was used as an internal standard.

ADDITIONAL RESOURCES

Supplemental information is available for this paper.